Experimental and theoretical study of the chemi-ionization in thermal collisions of Ne Rydberg atoms

P. O'Keeffe,[1] P. Bolognesi,[1] L. Avaldi,[1] A. Moise,[2] R. Richter,[2] A. A. Mihajlov,[3] V. A. Srećković,[3] and Lj. M. Ignjatović[3]

[1]*Consiglio Nazionale delle Ricerche - Istituto di Metodologie Inorganiche e dei Plasmi, Area della Ricerca di Roma 1, Monterotondo Scalo, Italy*

[2]*Sincrotrone Trieste Societá Consortile per Azioni, Area Science Park, I-34149 Basovizza (Trieste), Italy*

[3]*University of Belgrade, Institute of Physics, P. O. Box 57, RS-11001, Belgrade, Serbia*

(Received 28 February 2012; published 14 May 2012)

The state dependence of associative ionization of the *ns* and *nd* Rydberg series of Ne atoms with $5 < n < 18$ at thermal collision energies is investigated experimentally using a combination of synchrotron radiation and mass spectrometry in a single-beam experiment. The n dependence of the collisional and associative ionization of the Ne Rydberg atoms have been calculated using the dipole resonant mechanism, in particular the associative ionization rates for $5 < n_{\text{eff}} < 20$ have been calculated for cell, single beam, and crossed beam conditions. Refinements of the theory implemented previously have been necessary in order to apply the theory to the collisions of rare gas atoms. The results of the theoretical model for the n dependency of the associative ionization rates of the Ne Rydberg atoms are compared to the experimental data.

DOI: 10.1103/PhysRevA.85.052705 PACS number(s): 34.50.Fa, 31.50.Df, 32.80.Rm, 31.15.A−

I. INTRODUCTION

When an electron is excited into a high lying Rydberg state (large principal quantum number) even inelastic thermal collisions can be sufficiently energetic to lead to ionization reactions. These types of reactions can be classified under the general heading chemi-ionization reactions but can also be further broken down into classes depending on the products of the reaction. The possible processes for symmetric reactions are shown here:

$$A^*(n) + A \rightarrow A^+ + A + e^- \quad (1a)$$

$$A^*(n) + A \rightarrow A_2^+ + e^- \quad (1b)$$

where $A^*(n)$ represents a high n Rydberg state of an atom A and e^- is a free electron. Penning ionization is the term usually reserved for describing reactions of the type $A^*(n) + B \rightarrow B^+ + A + e^-$ where the ionization potential of atom (or molecule) B is less than the internal energy stored in $A^*(n)$. However in the case of reaction Eq. (1a) above the $A^*(n)$ Rydberg atom does not have enough energy to ionize the A atom collision partner and part of the ionization energy needs to come from the collision itself. Therefore in this work we will refer to this process as collisional ionization. The second process, called associative ionization (and its inverse reaction, dissociative recombination), although less studied with respect to Penning ionization is also the subject of an extensive literature. For a review of the evolution of the study of these types of reactions the reader is referred to Ref. [1] and references therein. Briefly one can classify the types of experiments performed into alkali Rydberg atom and rare gas Rydberg atom experiments. The former benefited greatly from the introduction of tuneable lasers, which could be used to photoexcite the Rydberg states of alkali metals in a precise manner with visible radiation. These methods paved the way for very controlled experiments on the collisions of Rydberg atoms of Li, K, Na, Rb, Cs in vapors [2,3], single beams [4,5], and cross beams [6–8], providing much information on the state and collision energy dependence of the reactions in Eqs. (1a) and (1b) for both the symmetric and asymmetric cases, where the symmetric case involves reactions between atoms of the same type while the asymmetric reactions are between a ground-state atom of one type and a Rydberg atom of another.

Generation of Rydberg states of rare gas atoms requires a much different approach as they lie at much higher excitation energies with respect to those of the alkali atoms. The earliest approach to this problem has been to use electric discharges in the gas in order to produce metastable excited atoms, which could be used to react with various targets. The population of the metastable states produced in this way is not extremely well controlled as a range of Rydberg states is populated in the discharge. To overcome this problem a number of approaches have been taken, for example, by combining the discharge source with laser excitation to allow a controlled photoexcitation of the high lying Rydberg states of rare gases starting from metastable states (e.g., in the case of Ne the $3s\ ^3P_{0,2}$ metastable atoms were employed) [9,10]. In this way Hotop and coworkers were able to investigate the state-selected collisional and associative ionization of rare gases in a precise way and the results obtained in this work will be compared with those experiments. Other techniques employed more recently include $2+1$ resonance enhanced multiphoton ionization (REMPI) using pulsed laser sources to excite individual Rydberg states of Xe atoms from the ground state combined with photoelectron spectrosopy to diagnose the collisional products [11,12]. Finally, Radler and Berkowitz [13] have excited Rydberg states of Ar in a one-photon process from the ground state using a VUV monochromator together with a Hopfield helium source for the excitation light. In this way they were able to examine the state dependence of the collisional and associative ionization of Ar Rydberg atoms. The experimental approach applied in this work is similar in concept to this method except that the one-photon VUV/EUV excitation source used here is the synchrotron radiation from Elettra, the Italian synchrotron source.

Also from the point of view of the theoretical description of the processes shown in Eqs. (1a) and (1b) great progress

 ©2012 American Physical Society

has been made in the last four decades. Indeed, a number of sophisticated models have been developed to describe these processes such as the Fermi mechanism [14], which treats the nonelastic process as being the result of the elastic scattering of the outer (Rydberg) electron on the atom-projectile. Within this mechanism the dipole moment of the the atom-projectile induced by the influence of the field of the Rydberg atom core is taken into account. However, the most successfully employed mechanisms have certain common ingredients. The basis of these descriptions is the resonant energy conversion within the electron component of the atom-Rydberg atom collision system, which is caused by the dipole part of the electrostatic interaction between outer electron of Rydberg atom and inner quasimolecular complex, consisting of the Rydberg atom core and the neutral ground state atom-projectile.

This mechanism, called the resonant mechanism, will be described in detail in Sec. III. Generally, this mechanism has been described by semiclassical methods such as the diffusion [15,16] or dipole (quasistatic) [17–19] models although a fully quantum model has also been attempted [20,21]. In this work we present the application of the dipole resonant mechanism to the collisions of rare gas atoms. The refinements that had to be made to the theoretical description to allow its application to the collisions of rare gas atoms are outlined in Sec. IV B.

Before proceeding to a detailed description of the experimental and theoretical methods employed it should be mentioned that the collisional processes studied here are relevant to the modeling of widely varying environments such as low-temperature plasmas [22] and, as has been suggested in a recent review [23], in the atmospheres of certain classes of stars.

Another area of research where the reactions investigated in this article have some relevance is that of the study of ultracold neutral plasmas. The formation of these plasmas were first demonstrated by the photoionization of ensembles of cooled Rydberg atoms of Xe [24] and subsequently it was found that Rydberg atoms are formed in expanding plasmas of this type [25,26]. Therefore it is clear that Rydberg atoms and their reactions have an important role in the formation and dynamics of ultracold plasmas.

II. EXPERIMENTAL METHODS

The experimental results described in this work were obtained at the branch line of the gas phase photoemission beam line at the Italian synchrotron light source, Elettra. The general layout of the beam line has been presented elsewhere [27] and therefore only a brief description is given here. The beam line optics setup is optimized to cover the soft x-ray range (below ∼250 eV), with all elements working at grazing incidence angles and most having gold coating.

A schematic of the experimental chamber is shown in Fig. 1. The synchrotron light was focused to a focal spot of circular shape with diameter 300 μm in the center of the reaction chamber. At this point pure neon gas was introduced into the chamber in the form of an effusive jet via a 6-cm long brass needle of internal diameter 250 μm. The amount of gas passing through the needle and thus the local pressure at the exit of the needle was controlled by a leak valve placed in the gas line behind which a pressure of 1 bar of gas was established. Pressure was varied by monitoring the base pressure of experimental chamber.

The ions formed in the collision processes in Eqs. (1a) and (1b) were extracted from the interaction region by ion optics and focused into a Balzers QMA 150 quadupole mass spectrometer where they were mass analyzed and detected by a secondary electron multiplier. Setting the quadrupole mass spectrometer to the center of a mass peak (e.g., mass = 40 a.m.u. for Ne_2^+) the efficiency of production of that ion could be monitored as a function of photon wavelength by scanning the beam line optics or of the pressure of gas in the effusive beam by varying the opening of the leak valve. The resulting scans were performed in sections of 200–300 meV changing the undulator gap to maximize flux at the central energy of each scan while monitoring the photon intensity using a photodiode.

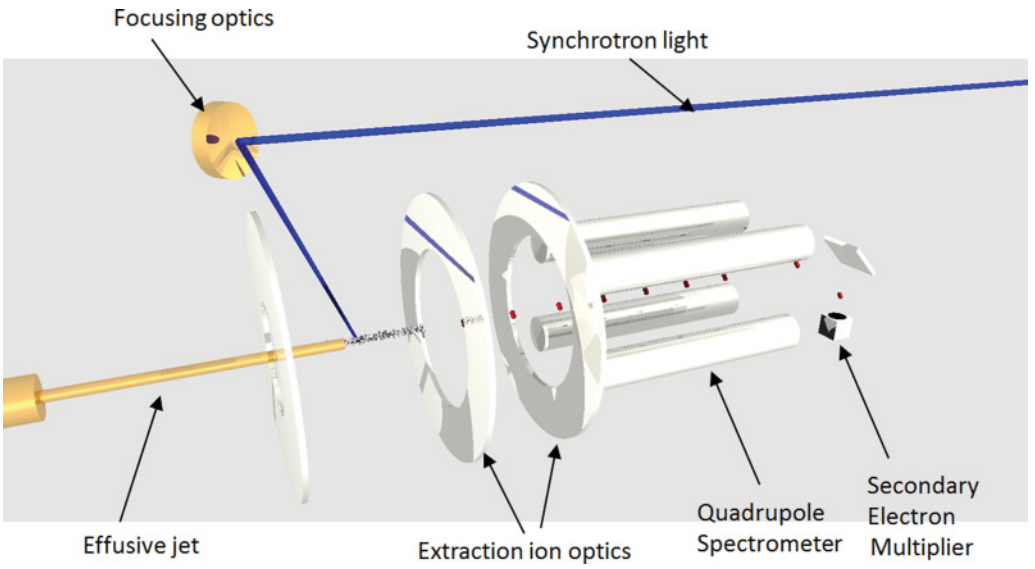

FIG. 1. (Color online) Schematic view of the geometry of the experimental setup. Details of the setup can be found in the text.

The intensity of each point was then corrected for the photon flux by dividing by the corresponding photodiode current. Each subscan overlapped with the adjacent scan in such a way as to have at least three peaks in common. Normalizing the intensity of adjacent scans then simply involved matching the areas of the peaks in the overlapping regions.

III. THEORETICAL DESCRIPTION OF THE CHEMI-IONIZATION REACTIONS

The basis of the theoretical description of the binary collisions of ground-state and Rydberg atoms used in this work is the dipole resonance mechanism (DRM). In this description of the chemi-ionization event it is envisaged that processes outlined in Eqs. (1a) and (1b) are induced by the dipole part of the electrostatic interaction between the outer Rydberg electron and the inner ion-atom system where the latter is considered to consist of the Rydberg atom core and the ground-state atom. In the description used here, this system is considered to be adequately described by the ion-ground state potential wells (i.e., the potential energy of the dimer cation).

The manner of application of the dipole resonant mechanism to the decay approximation according to Ref. [17] is characterized by several basic elements. First, it is assumed that the relative motion of the nuclei in $A^*(n) + A$ collisions is described by a classical trajectory characterized by the collision parameter ρ and the initial (collisional) energy E, such that: $\rho \ll r_n^2$, where r_n is the mean radius of the atom $A^*(n)$. Then, only such trajectories are taken into account that, for given n, ρ, and E, pass through the chemi-ionization zone, that is, the region: $R \leqslant R_{i,n}$, where R is the internuclear distance, and the boundary value $R_{i,n}$ is determined by the ionization energy I_n of the atom $A^*(n)$ and the corresponding parameters of the ion-atom subsystem $[A^*(n) + A]$.

Within this approximation the ion-atom subsystem is described by means of the electronic states of the corresponding molecular ions, $A_2{}^+$, denoted here as $|1,R\rangle$ and $|2,R\rangle$ and that

$$U_{12}(R) \equiv U_2(R) - U_1(R) > 0, \tag{2}$$

where $U_1(R)$ and $U_2(R)$ are the potential curves of the states $|1,R\rangle$ and $|2,R\rangle$ (see Fig. 2 for a graphical illustration of these curves). Here $|1,R\rangle$ is the ground electronic state of the molecular ion, or, in the general case, one from a group of states asymptotically correlated to the same state of the subsystem $A^+ + A$ at $R \to \infty$, to which the ground state is correlated.

Similarly, $|2,R\rangle$ is taken to be the first excited electronic state of the molecular ion, or, in the more general case, one from a group of excited states asymptotically correlated to the same state of the subsystem $A^+ + A$ at $R \to \infty$, to which the first excited state is correlated.

In the decay approximation the chemi-ionization processes are treated as a result of the transition

$$|2,R\rangle|n,l\rangle \to |1,R\rangle|k,l'\rangle \tag{3}$$

of the complete system from an initial state $|2,R\rangle|n,l\rangle$ to a final state $|1,R\rangle|k,l'\rangle$, which is caused by DRM. This event can be treated as a simultaneous transition of the outer electron and of the ion-atom subsystem, namely: $|n,l\rangle \to |k,l'\rangle$ and $|2,R\rangle \to |1,R\rangle$ respectively, which is illustrated in Fig. 2.

It is assumed that transitions (3) predominantly take place within narrow neighborhoods of the resonant points R_{nk} which are the roots of the equation: $\epsilon_{nk} \equiv \epsilon_k - \epsilon_n = U_{12}(R)$, where $\epsilon_k = (\hbar k)^2/2m_e$ and $\epsilon_n = -I_H/n^2$ are the energies of

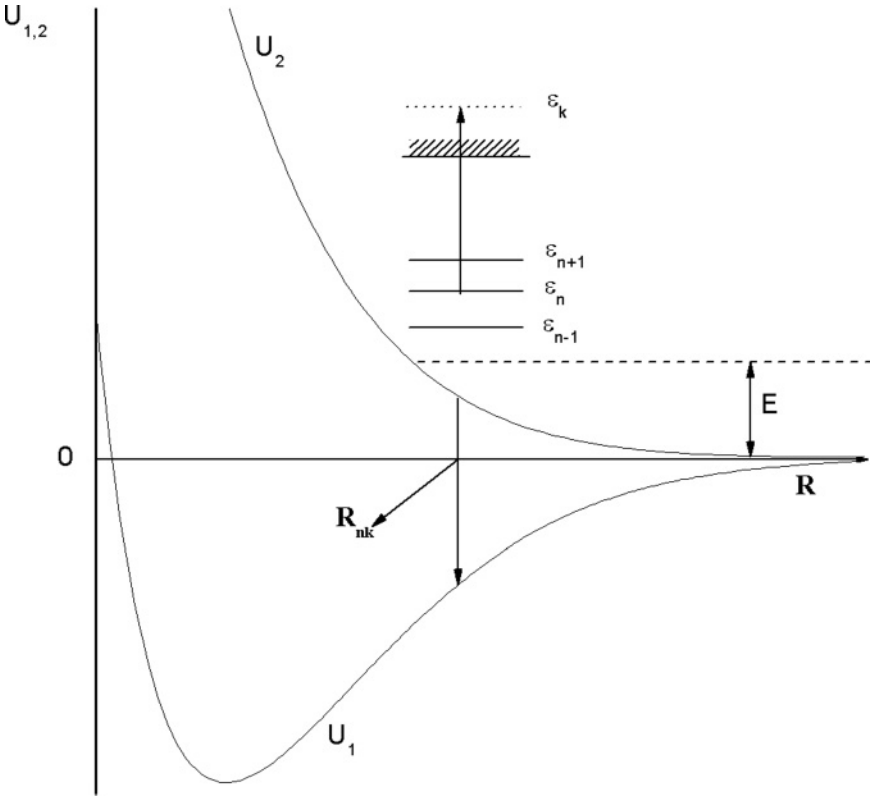

FIG. 2. Graphical illustration of the dipole resonant mechanism involving the simultaneous transition of the atom-Rydberg core system from the U_2 potential energy curve to the U_1 curve and emission of the electron into the continuum. E is the collision energy, ϵ_n are the energy levels of the Rydberg atom and ϵ_k is that of the electron in the continuum. The two one-sided vertical arrows indicate the simultaneous transition from the upper to the lower curve and the emission of the electron into the continuum (see text for further details).

the outer electron in the final (free) and the initial (bound) states and the splitting term $U_{12}(R)$ is defined by Eq. (2). During the collision the chemi-ionization process is described by the ionization rate $W_i(R;n,l)$, which implies that, for a given R the outer electron passes to the free state with energy $\epsilon_k(R) = U_{12}(R) + \epsilon_n$. In accordance with Janev and Mihajlov [17] the quantity $W_{i,n}(R)$ can be presented in the form

$$W_i(R,n,l) = \frac{4}{3\sqrt{3}n^5} D_{12}^2(R) G_{nk}(l),$$
$$D_{12}(R) = \langle 2,R|\hat{D}(R)|1,R\rangle, \tag{4}$$

where $\hat{D}(R)$ is the operator of the dipole momentum of the ion-atom subsystem, and $G_{nk}(l)$ is the corresponding (bound-free) Gaunt factor [28] (see below for definition), and the probability $P_{\text{chemi},n}(\rho,E)$ of the chemi-ionization event, for the considered ρ and E, is given by the relations

$$P_{i;n}(\rho,E) = p_{in}\left[1 - \exp\left(2\int_{R_{\min}}^{R_{i;n}} \frac{W_{i;n}(R)dR}{v_{\text{rad}}(R;\rho,E)}\right)\right],$$
$$v_{\text{rad}}(R;\rho,E) = \sqrt{\frac{2}{\mu}\left[E - U_2(R) - \frac{E\rho^2}{R^2}\right]}, \tag{5}$$

where $p_{in} = 1/2$ in the symmetric case and 1 in the nonsymmetric one, the lower integration boundary $R_{\min} \equiv R_{\min}(\rho,E)$ is the root of the equation: $v_{\text{rad}}(R;\rho,E) = 0$, and μ is the reduced mass of the system $A^+ + A$. It should be noted that the Gaunt factor $G_{nk}(l) \equiv \sigma_{\text{ph}}(n,l;k)/\sigma_{\text{ph}}^{\text{qc}}(n,l;k)$, where $\sigma_{\text{ph}}(n,l;k) \equiv \sigma_{\text{ph}}(n,l;k,l-1) + \sigma_{\text{ph}}(n,l;k,l+1)$, $\sigma_{\text{ph}}(n,l;k,l\pm1)$ is the cross section for the photoionization process $|n,l\rangle \to |n,l\pm1\rangle$, and $\sigma_{\text{ph}}^{\text{qc}}(n,l;k)$ is the corresponding quasiclassical (Kramer's) cross section.

Subsequently, the cross section $\sigma_{\text{chemi}}(E;n,l)$ for the chemi-ionization process under consideration and the corresponding rate coefficient $K_{\text{chemi}}(n,l;T)$ can be presented by means the usual expressions

$$\sigma_{\text{chemi}}(E;n,l) = \int_0^{\rho_{\max}(E,n)} P_i(\rho,E;n,l)2\pi\rho d\rho, \tag{6}$$

$$K_{\text{chemi}}(n,l;T) = \int_{E_{\min}(n)}^{\infty} \sqrt{\frac{2E}{\mu}}\sigma_{\text{chemi}}(E;n,l)f(E,T)dE, \tag{7}$$

where $f(E,T)$ is the corresponding distribution function over E at a given temperature T, which depends on the experimental conditions (a single beam, crossed beams, a cell). The parameters $\rho_{\max}(E,n) > 0$ and $E_{\min}(n) \geqslant 0$ are determined by the behavior of the potential curve $U_2(R)$ and the splitting term $U_{12}(R)$.

In order to describe both associative and collisional ionization channels we use the fact that $K_{\text{chemi}}(n,l;T)$ can be presented in the form

$$K_{\text{chemi}}(n,l;T) = K_{ai}(n,l;T) + K_{\text{colli}}(n,l;T), \tag{8}$$

where the associative ionization rate coefficient is given by

$$K_{ai}(n,l;T) = \int_{E_{\min}(n)}^{E_i(n)} \sigma_{ai}^{'}(E;n,l)f(E,T)dE + \int_{E_i(n)}^{\infty} \sigma_{ai}^{''}(E;n,l)f(E,T)dE, \tag{9}$$

while the collisional ionization rate coefficient $K_{\text{colli}}(n,l;T) \equiv K_{\text{chemi}}(n,l;T) - K_{ai}(n,l;T)$. In Eq. (9) the boundary energy $E_i(n)$ is equal to the ionization energy of the Rydberg atom under consideration [i.e., $E_i(n) = I_H/n^2$, and $\sigma_{ai}^{'}(E;n,l)$ and $\sigma_{ai}^{''}(E;n,l)$ denotes the corresponding associative ionization cross section]. Following the above analysis it can be seen that $\sigma_{ai}^{'}(E;n,l) \equiv \sigma_{\text{chemi}}(E;n,l)$, where $\sigma_{\text{chemi}}(E;n,l)$ is given by Eqs. (5) and (6), and $\sigma_{ai}^{''}(E;n,l)$ is given by the same expressions, but with the integration boundaries $R_{i;n}^{''}$ and $\rho_{\max}^{''}(E,n)$ instead $R_{i;n}$ and $\rho_{\max}(E,n)$. It can be shown that $R_{i;n}^{''}$ is equal to the root of the equation $U_{12}(R) = E$, and $\rho_{\max}^{''}(E,n)$ is the root of the equation $U_2(R_{\min}(\rho,E)) = E$.

IV. RESULTS

A. Experimental

The spectrum obtained by detecting Ne_2^+ from the overlap of a pure effusive jet of neon with photons in the energy range from 20.60 to 21.55 eV (just below the IP of Ne at 21.565 eV) with a Gaussian photon resolution of FWHM 0.55 meV is shown in Fig. 3.

Five Rydberg series are assigned and all peaks in the spectrum are identified. Three of these Rydberg series, $Ne^*(2p^5\,ns[3/2]_1)$, $Ne^*(2p^5\,nd[3/2]_1)$, and $Ne^*(2p^5 nd[1/2]_1)$ converge to the $Ne^+\ ^2P_{3/2}$ threshold while the remaining two, $Ne^*(2p^5\,ns'[3/2]_1)$, $Ne^*(2p^5\,nd'[3/2]_1)$, converge to the $Ne^+\ ^2P_{1/2}$ state of the ion. We use the convention of denoting Rydberg states converging to the higher threshold by a prime and the angular momentum coupling scheme used is jK coupling resulting in the $nl[K]_J$ Racah notation. Here $K = J_c + l$, $J = K + s$ where J_c is the total angular momentum of the core, l is the orbital angular momentum of the Rydberg electron and s is the spin angular momentum of the Rydberg electron.

The three traces reported in Fig. 3 are due to the spectrum being recorded at three different chamber pressures of 3.8×10^{-6}, 8.0×10^{-6}, and 1.5×10^{-5} mbar. The pressure in the interaction region is much higher than these readings.

Each peak in each spectrum has been fitted with a Gaussian function of fixed width (as the widths of the peaks are dominated by the resolution of the synchrotron radiation). The areas are plotted as a function of n_{eff} in Fig. 4, where $n_{\text{eff}} = n - \mu$, n being the principal quantum number of the Rydberg state and μ the corresponding quantum defect. The quantum defects have been taken from Ref. [29].

It is important to note that the probabilities of photoexcitation plus associative ionization reported here are not on an absolute scale as the errors associated with estimating gas density, photon intensity and spectrometer transmission efficiency were deemed too large in order to give a meaningful estimate of the absolute cross sections. However, n_{eff} of the same series can be compared and once the relative photoexcitation of the different series has been factored in also the relative associative ionization rates of the different Rydberg series can be compared (see Sec. V for a more complete discussion).

The extracted probabilities have been multiplied by factors of 4 and 13.3 for the pressures 3.8×10^{-6} and 8.0×10^{-6} mbar, respectively. This clearly shows a quadratic

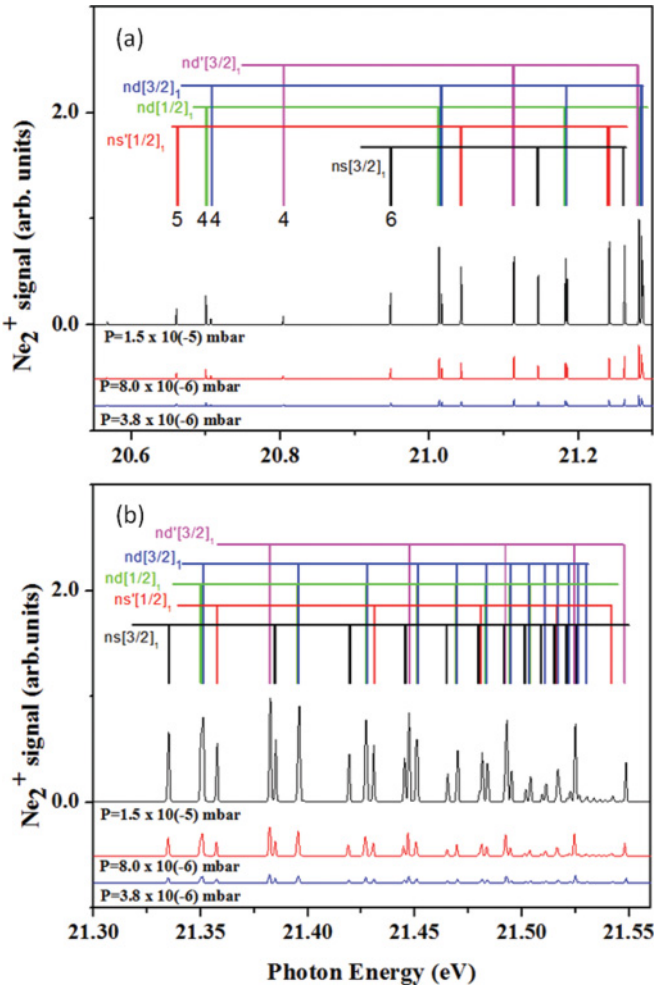

FIG. 3. (Color online) Pressure and wavelength dependence for the production of Ne_2^+ in a single effusive atomic beam. The pressures shown correspond to the base pressures of the chamber during the experiment. The spectra are divided into two photon energy regions: (a) 20.55–21.3 eV and (b) 21.3–21.56 and all spectra are renormalized such that the most intense peak (photon energy corresponding to excitation of the $Ne^*(2p^5\,6d'[3/2]_1)$ Rydberg state) in the $P = 1.5 \times 10^{-5}$ mbar spectrum has a maximum of 1. The relative intensities of the three spectra are respected.

pressure dependence of the process which is consistent with two-body collisions. Furthermore, an important point to note is that the dependencies on $n_{\rm eff}$ shown in Fig. 4 have exactly the same shape which suggest that radiative processes do not have an effect on the $n_{\rm eff}$ dependence of the collisional processes. This is because in the case that the radiative lifetimes of the Rydberg states were shorter or similar to the collision time then the radiative process would be in competition with the associative ionization rate. Furthermore, as the radiative lifetimes of the Rydberg states are proportional to $n_{\rm eff}^3$ then if the radiative decay competes with the associative ionization then a change in pressure (which modifies the collision time but not the radiative lifetime) should modify the AI rates of different n states in different ways. Since a change is not observed experimentally it can be concluded that the radiative decay does not affect the observed $n_{\rm eff}$ dependency of the AI rates.

B. Theory

Application of the theory outlined in Sec. III to the case of colliding neon atoms requires some refinement with respect to its application to collisions of alkali metals [18,19,30]. In particular since the electrons in the outer shell of the rare gas atom are in p states the ion-atom system can enter into the reaction zone not only in two Σ states but also in four Π states. The necessary potential energy curves for calculating $K_\Sigma(n,l;T)$ and $K_\Pi(n,l;T)$ were taken from Ref. [31].

Furthermore, the calculations also take into account the indirect channels in addition to the direct channel considered in Sec. III. The direct channel involves the approach along the reaction coordinate with the Rydberg electron in the $|n,l\rangle$ state and the ion-atom system in the $|2,R\rangle$ state (i.e., on the repulsive curve shown in Fig. 2) followed by simultaneous transition of both states induced by the DRM to $|k,l'\rangle$ (i.e., a continuum electron) and $|1,R\rangle$ (i.e., on the bound curve shown in Fig. 2). In an indirect channel the system is initially in the $|1,R\rangle|n,l\rangle$ state (i.e., entering into the collision region along the strongly bound dimer ion curve). The first step then involves DRM, which induces a simultaneous transition of the system to the $|2,R\rangle|n-1,l''\rangle$ state. Then finally the Rydberg electron (now in a different orbital with respect to the beginning of the collision) can escape into the continuum in the manner previously considered (i.e., $|2,R\rangle|n-1,l''\rangle \rightarrow |1,R\rangle|k,l'''\rangle$ again via the dipole resonant mechanism).

Consequently, the rate coefficients $K_\Sigma(n,l;T)$ and $K_\Pi(n,l;T)$ can be presented in form

$$\begin{aligned} K_\Sigma(n,l;T) &= K_\Sigma^{(1)}(n,l;T) + K_\Sigma^{(2)}(n,l;T), \\ K_\Pi(n,l;T) &= K_\Pi^{(1)}(n,l;T) + K_\Pi^{(2)}(n,l;T) \end{aligned} \tag{10}$$

where the indices 1 and 2 indicate the direct and indirect channels, respectively. The shift of the maxima of the indirect $K^{(2)}_{\Sigma,\Pi}(n,l;T)$ curves to smaller $n_{\rm eff}$ with respect to the maxima of the direct $K^{(1)}_{\Sigma,\Pi}(n,l;T)$ curves is caused only by the changes of the collision efficiency, while the chemi-ionization mechanism remains the same. First, together with the de-excitation transition $|n,l\rangle \rightarrow |n-1,l'\rangle$ of the Rydberg electron we have the transition of the inner quasimolecular complex from initial lower attractive electronic states with the energy $U_1(R)$ to the upper repulsive state $U_2(R)$. As a result, the Rydberg atom ionization energy becomes larger for the excitation energy $\epsilon_{n-1,n} = \mathcal{R}[1/(n-1)^2 - 1/n^2]$, but at the same time the kinetic energy of the collision system also becomes larger for the same energy $\epsilon_{n-1,n}$, without the change of the orbital moment of the system and with the increasing of the ionization barrier for the quantity which is less than $\epsilon_{n-1,n}/2$. This means that the gain of the kinetic energy of the collision system significantly surpasses the increase of the ionization barrier. The result is that the next phase of the chemi-ionization process, with the outer electron in the state $|n-1,l'\rangle$, with $l' = l \pm 1$, becomes energetically possible, but with the corresponding ionization zone shifted into the region of smaller internuclear distances R. In this phase two factors determine the ionization rate: the decrease of R, which causes a decrease of the rate ionization, and the decrease of the principal quantum number ($n-1$ instead n), which causes an increase of the rate ionization. It is clear that the final

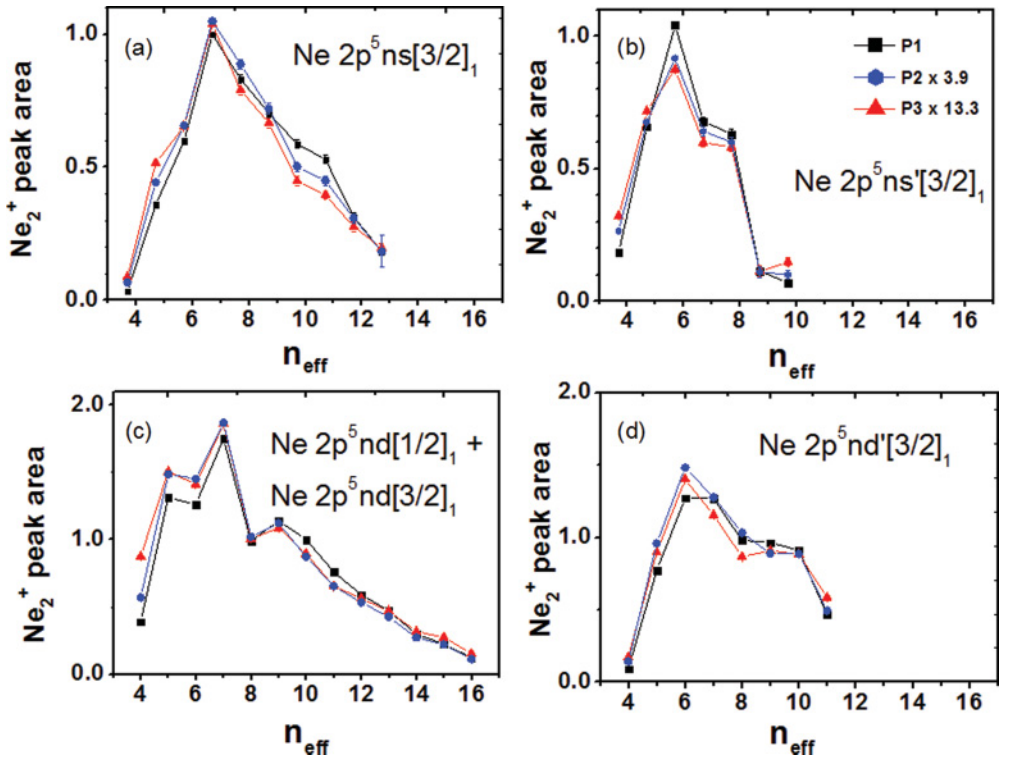

FIG. 4. (Color online) Graphs showing the peak areas extracted from the data in Fig. 3 for (a) the Ne*$(2p^5\,ns[3/2]_1)$, (b) Ne*$(2p^5\,ns'[3/2]_1)$, (c) the sum of Ne*$(2p^5\,nd[3/2]_1)$ and Ne*$(2p^5 nd[1/2]_1)$, and (d) the Ne*$(2p^5\,nd'[3/2]_1)$ Rydberg series. The peak areas extracted from the spectra in Figs. 3(a) and 3(b), using the fitting process described in the text, are plotted versus the effective principal quantum number $n_{\rm eff}$. Full squares, full circles, and full triangles correspond to the areas extracted from the spectra recorded with chamber pressures of 1.5×10^{-5}, 8.0×10^{-6}, and 3.8×10^{-6} mbar. The areas have been renormalized such that the area corresponding to the $n_{\rm eff} = 6.706$ of the Ne*$(2p^5\,ns[3/2]_1)$ series is equal to 1. Finally, the areas extracted from the spectra with chamber pressure of 8.0×10^{-6} and 3.8×10^{-6} mbar are multiplied by 3.9 and 13.3 respectively for the reasons discussed in the text.

probability of the overall process (for a given impact parameter and impact energy) strongly depends on the probability of the above mentioned transitions between the states of outer electron and inner quasimolecular complex. The total influence of these factors determines the shapes of the $K^{(2)}_{\Sigma,\Pi}(n,l;T)$ which are shown in Figs. 5(a) and 5(b). As can be seen from these figures the calculations predict that the indirect process contributes significantly to the AI rate for $n_{\rm eff} <$ 10–12 in the case of the Σ channel while it is always an order of magnitude less than the direct channel in the case of the Π channels.

The total associative ionization rate coefficients $K_{ai}(n,l;T)$ for the process in Eq. (1b) with $A =$ Ne have to be taken in the form

$$\begin{aligned} K_{ai}(n,l;T) &= K_{\rm chemi}(n,l;T)\cdot X_{ai}(T;n,l), \\ K_{\rm chemi}(n,l;T) &= \tfrac{1}{3}K_{\Sigma}(n,l;T) + \tfrac{2}{3}K_{\Pi}(n,l;T) \end{aligned} \tag{11}$$

where $K_{\Sigma}(n,l;T)$ and $K_{\Pi}(n,l;T)$ are the rate coefficients for reaction along the Σ and Π potentials, and $X_{ai}(n,l;T) = K_{ai}(n,l;T)/K_{\rm chemi}(n,l;T)$ is the branching coefficient which characterizes the relative contribution of the AI channel.

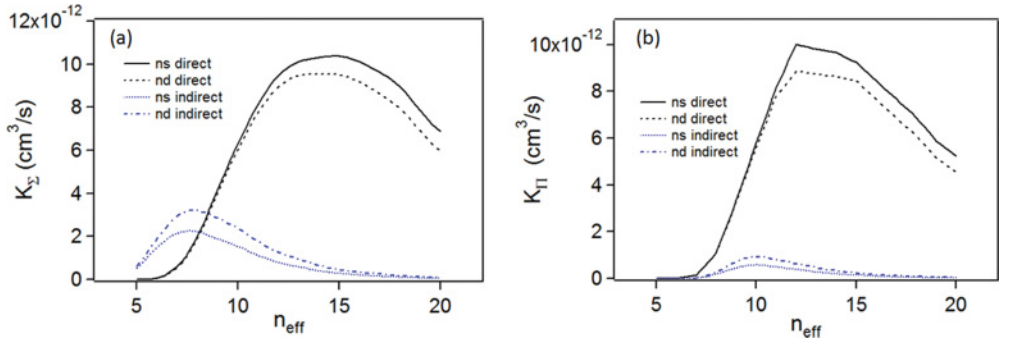

FIG. 5. (Color online) Comparison of the contributions of the reaction along curves of (a) Σ symmetry with that along curves of (b) Π symmetry for the direct and indirect processes for the collisions of s and d Rydberg atoms.

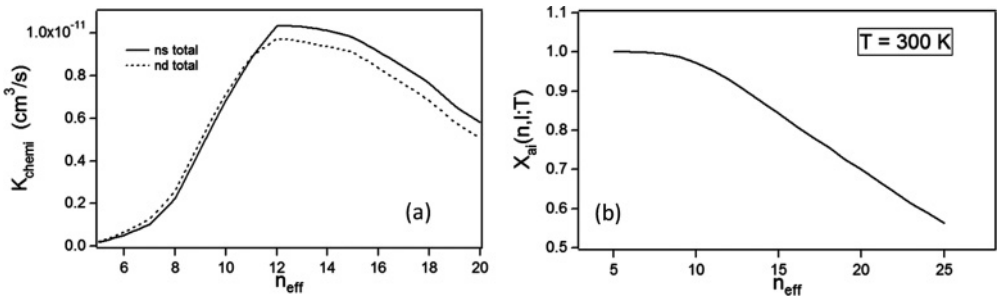

FIG. 6. (a) The total chemi-ionization rate as a function of $n_{\rm eff}$ obtained by summing the data in Fig. 5 according to Eq. (11) (b) the behavior of the branching coefficient $X_{ai}(n,l;T) = K_{ai}(n,l;T)/K_{\rm chemi}(n,l;T)$, characterizing the relative contribution of the AI channel, as the function of $n_{\rm eff}$.

V. DISCUSSION

The relative experimental associative ionization probabilities for the ns and nd series as a function of $n_{\rm eff}$ have been obtained from the peak areas shown in Fig. 4 in the following way: first, the relative intensities of the two series were corrected for the photoexcitation probabilities of the $Ne^*(2p^5\,6s[3/2]_1)$ state and the sum of the transition probabilities to the $Ne^*(2p^5\,5d[3/2]_1)$ and $Ne^*(2p^5\,5d[1/2]_1)$ states using the literature values [32] of 0.00330 and 0.00543, respectively, for the oscillator strengths for photoexcitation from the ground state. Then to account for the the $n_{\rm eff}^{-3}$ dependency of the photoexcitation probability of individual members within the Rydberg series [33] the values were multiplied by $n_{\rm eff}^3$. A good example where this intensity rule is observed is shown in Ref. [34] for the case of Ca $(5s5p\ ^3P_1) \rightarrow$ Ca $(5snd\ ^3D_2)$ transitions. The resulting data, which are shown as symbols in Fig. 7(a), represent the $n_{\rm eff}$ dependence of the associative ionization probability of the ns and nd Rydberg series on a relative scale. As stated in Sec. IV A determination of the density of the excited Rydberg states, density of ground-state atoms, and detection efficiency was deemed to be too subject to error in order to deduce the absolute cross section for the process with acceptable accuracy. Nonetheless it is possible to rescale these dependencies to the calculated values and compare the relative $n_{\rm eff}$ dependence of the associative ionization probability.

The calculated $n_{\rm eff}$ dependency of the associative ionization rate of the ns and nd Rydberg series under both single-beam and cell conditions are also shown in Fig. 7(a). It should be noted that these rates are on an absolute scale as shown on the right-hand vertical axis of the figure. To produce the curves of the rate coefficients versus $n_{\rm eff}$ the calculational method outlined in Sec. III has been followed using the relevant $f(E,T)$ expression in Eq. (7) for the single-beam [30] and cell conditions (Maxwell distribution) at 300 K. The resulting total chemi-ionization rates were then converted into the associative ionization rates using the branching coefficients shown in Fig. 6(b).

Before comparing these calculated results with the experimental data it is interesting to comment on the differences in the behavior of the AI rate coefficients for single-beam and cell conditions. These differences are principally due to the different velocity/energy distribution functions $f(E,T)$ mentioned above, which in the case of the cell conditions is a Maxwell distribution, which peaks at $\sim kT$ while that of the single beam peaks at zero energy. The result is that in the case of the cell the lower $n_{\rm eff}$ (requiring high-energy collisions as the ionization energy is large) have a higher rate coefficients than the equivalent $n_{\rm eff}$ in the case of the single beam while the reverse is true for high $n_{\rm eff}$ with a crossing point occurring at $n_{\rm eff} = 10$ [see Fig. 7(b)].

In order to further test the theoretical methods employed here further calculations of the $n_{\rm eff}$ dependence of the

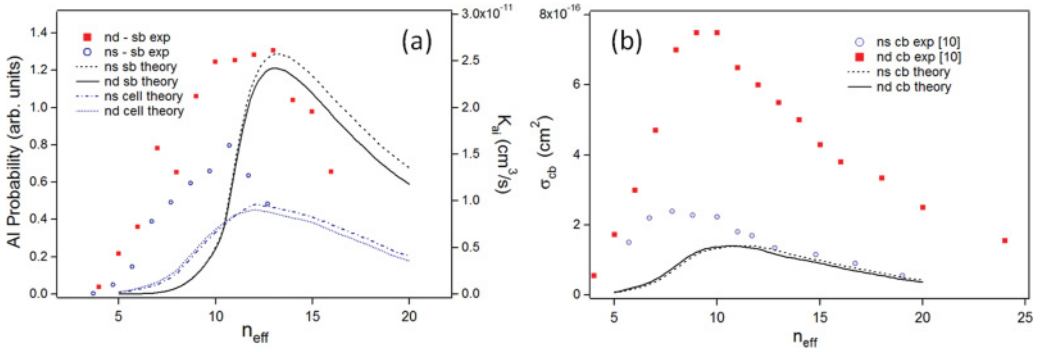

FIG. 7. (Color online) (a) Experimental data (symbols) for the relative associative ionization rates of the ns and nd Rydberg series of Ne under single-beam (sb) conditions together with the calculated values (lines) for both the single-beam and cell conditions and (b) experimental data (symbols) for the absolute associative ionization cross sections of the ns and nd Rydberg series of Ne under crossed beam (cb) conditions taken from Ref. [10] together with the calculated values (lines) for crossed beam conditions.

associative ionization cross section under crossed beam conditions again using the procedure outlined in Sec. III have been done. The only difference with respect to Fig. 7(a) is that the rate coefficients have been converted into cross sections. The theoretical results (lines) are compared with the absolute cross sections obtained by Harth *et al.* [10] by measuring the target gas density flux using a viscosity manometer and the Rydberg excited state density using a combination of the Ne^+ signal produced by blackbody radiation and the reduction in the metastable density due to the laser excitation. Therefore, both theory and experiment are graphed on common absolute scales in this case.

The experimental data for the AI rates for both single [Fig. 7(a)] and the crossed beam conditions [10] [Fig. 7(b)] show that the AI rates for the nd series is greater than that of the ns series in the entire measured range. Furthermore, the maxima of the AI rates as a function of n_{eff} of the crossed beam experiment is shifted to slightly lower n_{eff} with respect to the single-beam conditions (max $n_{\text{eff}} = 9$–10 for the nd series in the crossed beam case versus max $n_{\text{eff}} = 11$–12 for the single-beam conditions.). As discussed above this effect is reflected in the calculated rates and is due to the different velocity distributions involved in the two experiments. From the point of view of the absolute cross-section values shown in Fig. 7(b) the theory is in agreement with the AI rates for the ns series for $n_{\text{eff}} > 12$.

On the other hand, both the single and the crossed beam cases the experimental results indicate that the associative ionization cross sections for the nd series are significantly larger than those for the ns series while the theoretical curve are very similar. From an experimental point of view the crossed beam results gives an nd to ns associative ionization rate ratio of $\sim$4 while the single-beam results show a value of $\sim$1.5 for this ratio for Rydberg states with $n_{\text{eff}} > 9$. The estimated error in the case of the single-beam experiment is principally related to the procedure used to correct for the n_{eff} dependency of the photoexcitation probability of the reacting Rydberg states (multiplication by n_{eff}^3) while that of the crossed beam experiment is estimated to be $\pm 50\%$. In the cross beam case [10] the Rydberg population has been measured and the photoexcitation probability is not required in the correction. The difference in the ratio between the two experimental measurements may also be related to the fact that the Rydberg series probed have different total J with the Rydberg series in the single-beam experiments having $J = 1$ while those in the crossed beam experiments have $J = 2$ although a definitive conclusion is not possible considering the experimental uncertainties.

Nonetheless it is clear that in both experimental cases the nd series AI rate is significantly larger than that of the ns series, which is not reflected the in theoretical results. In the theory description outlined in Sec. III it can be seen that the same potential curves are used for the calculation of the AI rates of both the ns and nd series. The only difference is due to the upper boundary of the region of internuclear distances which are relevant for the AI process for a given n and l, which depends on the ionization energy of the Rydberg state in question. As the ns and nd Rydberg states of similar n_{eff} have almost identical ionization energies this part of the model gives almost identical factors for these states. Therefore, within this model large differences between the AI rates of different Rydberg series may only be attributed to the Gaunt factor in Eq. (4) This because the AI rate is directly proportional to the Gaunt factor which is, in turn, the ratio of the photoionization cross section to the Kramers quasiclassical cross section. Indeed, the calculated Gaunt factors show that $G_{ns} < G_{nd}$ for $n < 10$ while $G_{ns} > G_{nd}$ for $n > 10$, which is exactly reflected in the relative AI rates of the ns and nd series (see Fig. 7). Therefore, a possible reason for this discrepancy between theory and experiment is that the Gaunt factors for the nd series are underestimated. The Gaunt factors employed here are calculated as described in Sec. III using the photoionization, σ_{ph}, and Kramer's quasiclassical, $\sigma_{\text{ph}}^{\text{qc}}$, cross sections. The $\sigma_{\text{ph}}(n,l;k,l\pm 1)$ values used are those calculated for the hydrogen atom with the influence of the real multielectron structure of the considered atom taken into account by the use of the n_{eff} and thus the quantum defect of the Rydberg state. The existing disagreement between the calculated and experimentally measured ratios of the AI rates of the ns to nd series shows that these approximations may be insufficient for the describing of the considered AI process in the lower part of the Rydberg region ($n \lesssim 10$). Furthermore, it should be noted that different AI rates for different total J series could also be explained by different cross sections for photoionization of these series into the continuum.

Finally, also quite clear in both the single and crossed beam cases [Figs. 7(a) and 7(b), respectively] is that the theoretical model employed here underestimates the AI rates for $n_{\text{eff}} < 12$. One observation that can be made by examining Fig. 5 is that the indirect channel contributes to the AI rates exactly in the region $8 < n_{\text{eff}} < 12$. Therefore, it is possible that this channel is underestimated in the model as by simply increasing the contributions of this channel agreement with the experiment would improve significantly.

VI. CONCLUSION

In this work we present experimental results on the relative n_{eff} dependency of the associative ionization rates of the ns and nd series in Ne. The experiments have been performed in a single beam configuration using tunable synchrotron light to selectively excite the $Ne^{**}(nl)$ atoms. These atoms then underwent AI within the beam and the resulting Ne_2^+ ions were detected. The theoretical model used in this work to describe this process is based on the dipole resonant mechanism where the ionization is treated as an excitation of the Rydberg electron into the continuum due to a quasiresonant exchange of energy with the electronic component of the atom-Rydberg atom system. This can in some ways be considered as a virtual photon exchange. Therefore, the overall process can be seen as a two-photon process in which the first photon is provided by the synchrotron radiation while the second is the virtual photon exchanged in the collision process. A number of modifications to the DRM model used to describe alkali metal associative ionization reactions had to be made in order to apply the model to the collision of rare gases. In particular, since the electrons in the outer shell of the rare gas atom are in p states the ion-atom system it is necessary to account for the reaction of the system not only on two Σ states but also on four Π states. Also, an indirect channel, which involves a

double curve hopping mechanism, was taken into account in the DRM model for the first time.

To compare the AI rates calculated using the DRM model with the experimental results we first removed the photoexcitation probability dependencies of the high lying Rydberg states. The calculated rates for the single-beam conditions were then compared to the experimental results presented in this work while those calculated for crossed beam conditions were compared to the experimental results of Harth *et al*. [10]. The experimental associative ionization rates in the single beam experiment peak at higher values of n_{eff} with respect to the crossed beam experiment. This behavior is reflected in the calculated rates and is due to the different velocity distributions in the two calculations. The calculated values for the absolute associative ionization cross sections are in agreement with the experimental measurements on the *ns* series in the crossed experiments. However, disagreement was observed between the calculated and experimental ratio of AI rates for the *nd* series with respect to the *ns* series and also the theoretical rates are underestimated with respect to the experimental rates for $n_{\text{eff}} < 12$ in both single and crossed beam cases. Possible reasons for these discrepancies involving the Gaunt factor and the possible underestimation of the indirect channel are discussed in detail.

ACKNOWLEDGMENTS

The authors thank the Susanna Piccirillo for a loan of the quadrupole mass spectrometer used in these experiments. This research was partly the Italian Research Project of National Interest (PRIN), Projects No. 2009W2W4YF and No. 2009W2W4YF. Also, this work was supported by the Ministry of Education and Science of the Republic of Serbia within the Projects No. 176002 and No. III44002.

[1] A. N. Klucharev and V. Vujnović, Phys. Rep. **185**, 55 (1990).
[2] C. E. Burkhardt, W. P. Garver, V. S. Kushawaha, and J. J. Leventhal, Phys. Rev. A **30**, 652 (1984).
[3] L. Barbier and M. Cheret, J. Phys. B **20**, 1229 (1987).
[4] J. Weiner and J. Boulmer, J. Phys. B **19**, 599 (1986).
[5] I. I. Ryabtsev, D. B. Tretyakov, I. I. Beterov, N. N. Bezuglov, K. Miculis, and A. Ekers, J. Phys. B **38**, S17 (2005).
[6] P. Polak-Dingels, J. Keller, J. Weiner, J.-C. Gauthier, and N. Bras, Phys. Rev. A **24**, 1107 (1981).
[7] J. Weiner and P. Polak-Dingels, J. Chem. Phys. **74**, 508 (1981).
[8] J. Boulmer, R. Bonanno, and J. Weiner, J. Phys. B **16**, 3015 (1983).
[9] H. Hotop, J. Lorenzen, and A. Zastrow, J. Electron Spectrosc. Relat. Phenom. **23**, 347 (1981).
[10] K. Harth, H. Hotop, and M. W. Ruf, International Seminar on Highly Excited States of Atoms and Molecules **101**, 117 (1986).
[11] X. K. Hu, J. B. A. Mitchell, and R. H. Lipson, Phys. Rev. A **62**, 052712 (2000).
[12] R. H. Lipson, X. K. Hu, J. B. A. Mitchell, and C. Froese-Fischer, Phys. Rev. A **68**, 012717 (2003).
[13] K. Radler and J. Berkowitz, J. Chem. Phys. **70**, 221 (1979).
[14] E. Fermi, Nuovo Cimento **11**, 157 (1934).
[15] N. Bezuglov, V. Borodin, A. Kazanskii, A. Klyucharev, A. Matveev, and K. Orlovskii, Opt. Spectrosc. **91**, 19 (2001).
[16] K. Miculis, I. I. Beterov, N. N. Bezuglov, I. I. Ryabtsev, D. B. Tretyakov, A. Ekers, and A. N. Klucharev, J. Phys. B **38**, 1811 (2005).
[17] R. K. Janev and A. A. Mihajlov, Phys. Rev. A **21**, 819 (1980).
[18] L. M. Ignjatović, A. A. Mihajlov, and A. N. Klyucharev, J. Phys. B **41**, 089801 (2008).
[19] L. M. Ignjatović, A. A. Mihajlov, and A. N. Klyucharev, J. Phys. B **41**, 025203 (2008).
[20] E. L. Duman and I. P. Shmatov, J. Exp. Theor. Phys. **51**, 1061 (1980).
[21] V. S. Lebedev, J. Phys. B **24**, 1993 (1991).
[22] N. Popov, Plasma Phys. Rep. **35**, 436 (2009).
[23] Y. Gnedin, A. Mihajlov, L. Ignjatović, N. Sakan, V. Srećković, M. Zakharov, N. Bezuglov, and A. Klycharev, New Astron. Rev. **53**, 259 (2009).
[24] T. C. Killian, S. Kulin, S. D. Bergeson, L. A. Orozco, C. Orzel, and S. L. Rolston, Phys. Rev. Lett. **83**, 4776 (1999).
[25] T. C. Killian, M. J. Lim, S. Kulin, R. Dumke, S. D. Bergeson, and S. L. Rolston, Phys. Rev. Lett. **86**, 3759 (2001).
[26] R. S. Fletcher, X. L. Zhang, and S. L. Rolston, Phys. Rev. Lett. **99**, 145001 (2007).
[27] R. R. Blyth, R. Delaunay, M. Zitnik, J. Krempasky, R. Krempaska, J. Slezak, K. C. Prince, R. Richter, M. Vondracek, R. Camilloni, L. Avaldi, M. Coreno, G. Stefani, C. Furlani, M. De Simone, S. Stranges, and M.-Y. Adam, J. Electron Spectrosc. Relat. Phenom. **101–103**, 959 (1999).
[28] W. Karzas and R. Latter, Astrophys. J. Suppl. **6**, 167 (1961).
[29] M. Baig and J. P. Connerade, J. Phys. B **17**, 1785 (1984).
[30] L. M. Ignjatović and A. A. Mihajlov, Phys. Rev. A **72**, 022715 (2005).
[31] T. Ha, P. Rupper, A. Wuest, and F. Merkt, Mol. Phys. **101**, 827 (2003).
[32] W. F. Chan, G. Cooper, X. Guo, G. R. Burton, and C. E. Brion, Phys. Rev. A **46**, 149 (1992).
[33] J. Berkowitz, *Photoabsorption, Photoionization, and Photoelectron Spectroscopy*, Pure and Applied Physics Series (Academic Press, New York, 1979).
[34] A. Nadeem and S. Haq, Specrochim. Acta B: Atomic Spectroscopy **65**, 842 (2010).